Chapter

Effect of Processing and Orientation on Structural and Mechanical Properties of Polypropylene Products

Luca Fambri and Luca Lutterotti

Abstract

Polypropylene (PP) represents one of the most worldwide used plastics with a large variety of products and applications. As usual for semicrystalline polymers, the properties of PP products strictly depend on the processing (fiber spinning, film extrusion, injection, etc.), where orientation and crystallization phenomena are involved. The object of this communication is the mechanical and structural characterization of oriented products from iPP homopolymers, i.e., injection molded dumbbell specimens (IM), lab-scale single fibers and commercial bulk continuous filament (BCF), woven non-woven fabrics (WNW) by using differential scanning calorimetry (DSC), dynamical mechanical thermal analysis (DMTA), tensile measurements, and X-ray diffraction (XRD) analysis. In particular, a recent methodology to analyze diffraction images of oriented polymers to obtain crystal structure, texture, and microstructural information is presented. The higher the orientation, the higher the mechanical properties and the sharper the texture, as revealed by a quantitative texture analysis that has been also developed and successfully applied to oriented PP nanocomposites.

Keywords: fibers, woven non-woven fabrics, tensile properties, DMTA, DSC, XRD analysis

1. Introduction

On the market volume basis of standard plastics, polypropylene occupies the second position after various polyethylenes (HDPE, LDPE, and LLDPE) and is expected to rise by 3% per year by 2024 according to the recent report by Ceresana [1]. Following PlasticsEurope about 9.9 m of PP were demanded in 2017 for food packaging, sweet and snack wrappers, hinged caps, microwave containers, pipes, automotive parts, bank notes, etc. in Europe [2]. The success of polypropylene derives from the proper balanced physical and chemical properties with a combination of many factors, such as low density, excellent thermal stability, good chemical resistance, high crystallinity, and high stiffness or hardness with a wide design flexibility and simplicity of recycling making PP an attractive construction material. Owing to plausible melt rheology and thermal properties, PP-based materials are compatible with many processing technologies and can be processed by injection molding, film blowing and casting, extrusion of woven non-woven fabrics,

fiber spinning, and calendering [3, 4]. Also polypropylene composites for injection molding represent a sector of production for applications where higher stiffness and hardness are required. These higher mechanical properties are often obtained by addition and dispersion of particulate fillers and/or glass fibers [5].

Depending on the process and applications, various grades of polymer are properly selected and defined by melt flow index (MF) that represents the output of polymer expressed in g/10 mins during a vertical extrusion and measured in standard conditions, usually at 230°C and load of 2.16 kg with a diameter die of 2.096 mm [6]. @@@Melt flow grades in the range 0.3–2.0 are chosen for pipes, sheets, and blow molding, whereas higher grades between 2 and 8 are selected for film and fiber production. Higher fluidity polymers with MF above 8 are typically used for injection molding and extrusion coating [7]. Common MF for woven non-woven (WNW) fabrics is usually in the range 18–25.

During various processing conditions, polymer chains are oriented, and the final properties directly depend on the combined interaction of polymer crystallized and amorphous phases during shear flow and/or elongational flow. The latter is typically dominating in film and fiber production. In particular, it is possible to achieve a high extension of macromolecular chains due to the relatively easy spinning, with a very high level of alignment [8, 9]. According to Kunugi, experimental maximum modulus and strength of about 40 and 1.5 GPa, respectively, could be obtained for highly extended helix crystallizing polymer [10]. In the case of injection molded polypropylene, an extensive work has been published with specific details on the effect of macromolecular orientation on polymer structure, after process, characterized by XRD, DSC, and DMTA in dependence on various factors, such as skin layer, filler effect, copolymers, flow direction, processing parameters, etc. [11].

In this chapter both injection molded samples and fiber-based products are compared as function of polymer processing. Mechanical, thermal, and structural analyses are presented. Particular attention will be spent on interpretation of X-ray analysis on fiber oriented polymers, comparing results before and after mechanical and creep tests.

2. Experimental

2.1 Products and polymers

Various products of PPs with different MF in the range 3.6 and 18 g/10 mins were selected and analyzed for the comparative evaluation of the effect of process on properties and orientation. The higher the molecular weight, the lower the melt flow. **Figure 1** shows the empirical relation between molecular weight and melt flow according to literature data [12] and Eq. (1):

$$\log MW = 2.47 - 0.234 \log MF \quad (1)$$

where MW is the molecular weight expressed in kDalton and MF is the melt flow measured in standard conditions (230°C and 2.16 kg). The MF value of polypropylene of various products is also reported. See details in **Table 1**.

Dumbbell specimens ASTM type (3.2 thickness, 12.7 width) were obtained by injection molding machine Arburg 320 C type Allrounder 500–250 (screw 35 mm) from iPP HP551M (Basell, Ferrara; MF ≈ 8 g/10 mins). Processing conditions were injection velocity of 40 cm^3/s, melt temperature (nozzle) of 240°C, and injection pressure 1100 bar.

WNW fabrics with surface density of 80 g/m^2 were spunbonded by Texbond Spa (Rovereto, TN, Italy) by using iPP with melt flow of 18 g/10 mins (at 2.16 kg

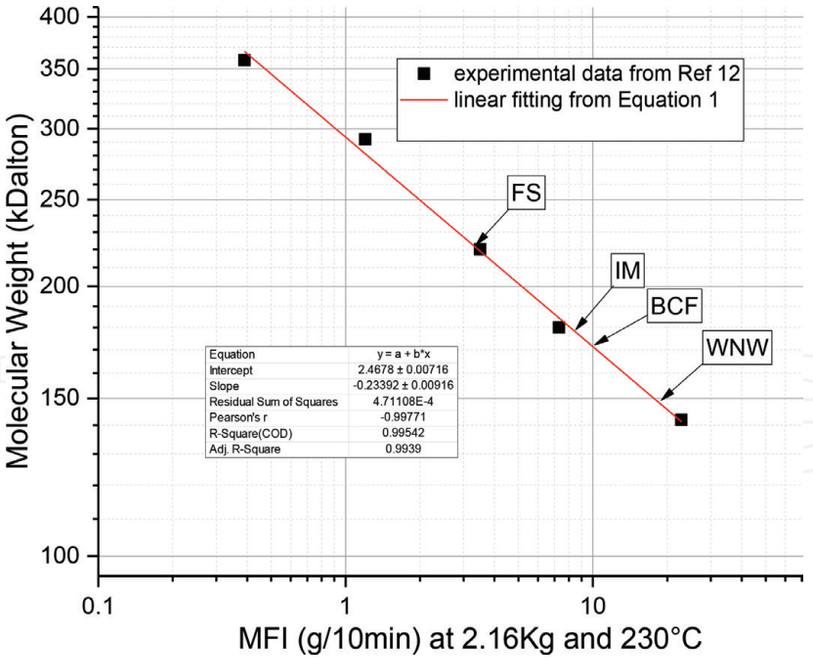

Figure 1.
Relation between melt flow index and molecular weight. The value of various products are indicated, i.e., woven non-woven (WNW), bulk continuous filaments (BCF), injection molding (IM), and fiber spinning (FS).

Code	Product	MF g/10 mins	Process
FS	Monofilament	3.6	Fiber spinning
IM	Dumbbell	8.5	Injection molding
WNW	Fabrics	18	Woven non-woven spunbonding
BCF	Multifilament	10.0	Bulk continuous filament spinning

Table 1.
Products obtained from polypropylene of different melt flow.

and 230°C). Due to the anisotropy of the process, fabrics were tested in machine direction (MD) and cross direction (CD) [13]. Normalized thickness of samples for mechanical testing was obtained assuming 0.905 g/cm as bulk density of polymer.

BCF of 64 filaments with the total titer of 1150 dtex [14] and equivalent diameter of 403 μm were industrially produced by Aquafil Spa (Arco, TN, Italy) by using PP with melt flow of 10 g/10 mins (2.16 kg, 230°C).

Monofilaments of PP and composite fiber were produced in lab-scale starting from commercial pellets (Sabic PP505P with MF = 3.6 g/10 mins at 2.16 kg and 230°C) and kaolinite masterbatch (Paralux by Vale, Brazil). Polypropylene fibers containing kaolinite in the range 1–30 wt% were manufactured by a two-step process, i.e., compounding/melt spinning and hot drawing. Melt-compounding was performed in a corotating intermeshing twin-screw extruder Rheomix Thermo Haake PTW16 (L/D 25; D = 16 mm; rod die 1.65 mm; temperature profile 130–230°C). Drawing of extruded filaments with 500 μm diameter was set at 145°C in order to produce single fiber at increasing draw ratio (DR) in the range 5–15. More details of compounding-spinning-drawing processes are described in literature [15, 16].

2.2 Mechanical and thermal tests

Tensile tests were performed on dumbbell ASTM specimens (Section 3.2 × 12.7 mm), BCF multifilaments (200 mm length), and WNW fabrics (50 mm width and 200 mm

length) by using a dynamometer Instron mod. 4502 with a crosshead speed of 100 mm/min. WNW fabrics were tested both in machine and in cross direction. Single fibers of 10–20 mm were tested with a crosshead of 5–10 mm/min.

Differential scanning calorimetry was performed on PP specimens of about 15 mg by means of a Mettler DSC30 calorimeter by thermal cycling in the range 0–220°C with a heating/cooling rate of 10°C/min. Melting and crystallization temperature/peak were registered. The crystallinity X was determined referring the measured melting enthalpy ΔH_i in the first heating scan to 207 J/g and the standard enthalpy of the fully crystalline PP according to Eq. (2):

$$X = 100\ \Delta H_i/207. \quad (2)$$

DMTA-thermal creep specimens of WNW (stripes 20x5 mm) and BCF (15 mm length) were subjected to dynamical mechanical analysis in tensile mode by using a DMTA Mk II (Polymer Laboratories) with a dynamic deformation of 11 μm, frequency of 5 Hz, static stress between 1 and 16 MPa, and heating rate of 3°C/min in the range −50/120°C. Storage (E') and loss (E") moduli are reported as a function of temperature. Thermal creep (TC) was also evaluated according to Eq. (3):

$$TC = 100^{*}(\Delta L/L_0) \quad (3)$$

where ΔL is the specimen length variation and L_0 is the initial length.

Isothermal creep at 25°C was performed on samples 200 mm length (and 50 mm width for WNW fabrics) by applying for 30 mins a constant stress of 16 MPa for BCF and 3.5 MPa for WNW, and a following recovery for 30 mins at a minimum stress of 1.5 MPa for BCF and 0.05 MPa for WNW, respectively. WNW fabrics were tested both in machine and cross direction.

2.3 Fiber diffraction measurements

All diffraction images were collected in transmission using a modified Laue camera with a removable image plate 24 × 15 cm^2 with a pixel size of 43 microns at a distance from the sample equal to 8.81 cm. The sample to detector distance

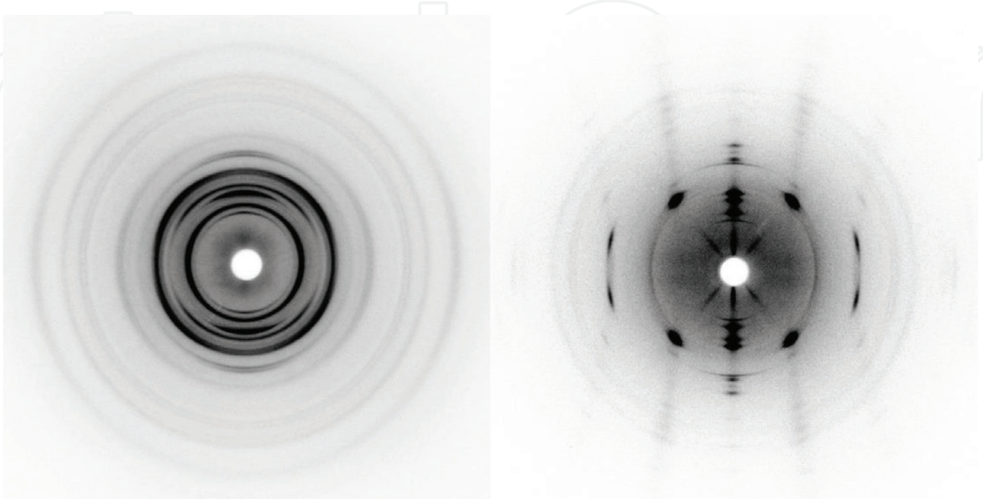

Figure 2.
Fiber diffraction raw images for the PP fibers with 10 wt% kaolinite (K10). (a) As-span fibers showing smoother texture. (b) Fibers at DR = 10: the central spots radially dispersed are due to diffraction from the residual bremsstrahlung radiation in the filtered only X-ray beam. Sharper spots are produced by the PP strong fiber texture, and more continuous circles are from kaolinite diffraction.

was calibrated through a Si standard powder packed between two Mylar films and stretched by the same fiber diffraction sample holder used for the polymers.

The beam (CuKα radiation at 40 kV and 30 mA) was collimated through a pinhole and a Ni filter to ensure a proper resolution in the images and sufficient beam intensity. Only one diffraction image per sample was sufficient to get all the crystal, texture, and microstructure information needed.

In **Figure 2(a)** and **(b)**, two of these diffraction images are shown for the PP fibers with kaolinite filler. The two images enlighten how easily the differences in texture can be caught by the fiber diffraction technique. Not only the quality of the texture can be appreciated but also a quantitative analysis can be done by a proper methodology shown in the following paragraph. From the two images, we can also see some artifacts originated from the not strictly monochromatic beam (diffraction of the bremsstrahlung), but we account for them in our analysis.

3. Results and discussion

3.1 Mechanical properties

The effect of orientation of various polypropylene products can be firstly evaluated by the different mechanical properties; in particular modulus and maximum stress (strength) are summarized in **Figure 3**.

Dumbbell specimens exhibited a tensile modulus of 950 ± 9 MPa, yield stress of 33 ± 1 MPa, and stress and deformation at break of 15 ± 2 MPa and 73%, respectively. Mechanical properties are quite different from other products, even if molecular weight is quite similar to BCF products. In injection molding, chain alignment and solidification follow a different pattern with respect to the fiber formation during spinning, and consequently dumbbell specimens exhibit heterogeneity in macromolecular orientation with a skin effect and a disordered core structure, as well described in literature [11]. Moreover, it should be considered that the shape factor, calculated as the ratio between the perimeter and section, is lower for IM (0.8 mm^{-1}) with respect to 160 mm^{-1} for WNW, 80 mm^{-1} for BCF, and in the range of 8–31 mm^{-1} for FS depending on the drawing. The efficiency of chain orientation

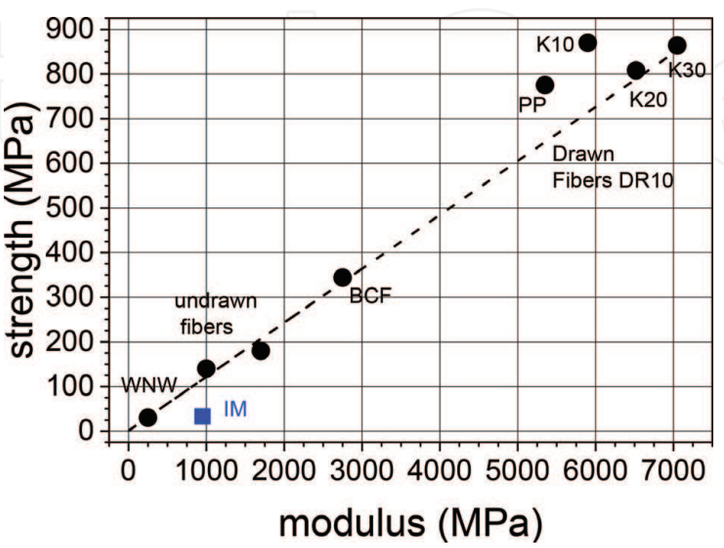

Figure 3.
Comparison of mechanical properties (tensile modulus and strength) of various oriented products, such as WNW, undrawn fibers from WNW, BCF, and drawn fibers with DR = 10; selected data of PP fibers or nanocomposite fibers with 10 (K10), 20 (K20), and 30% (K30) of kaolinite. Data of IM sample are also shown for comparison.

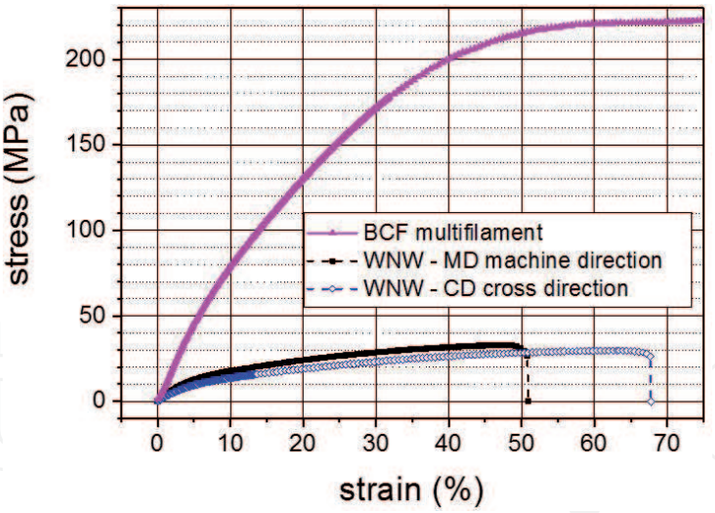

Figure 4.
Comparison of stress-strain curves of BCF filament and WNW fabrics tested in MD and CD directions.

is more evident in fiber-like products, where processing conditions determine a linear stretching (drawing) of polymer with elongation flow, either in spinning or in drawing.

The higher the orientation, the higher the modulus, the higher the strength, and in general the lower the strain at break. It is evident of the lower values of WNW fabrics with respect to undrawn fibers and BCF filaments. An almost linear dependence between strength and stiffness can be observed in **Figure 3**.

The highest modulus and strength have been obtained for lab-scale fiber after drawing 10 times (DR10) and relatively higher values for nanocomposites with kaolinite between 10 and 30%.

Stress-strain curves of WNW fabrics and BCF filaments are shown in **Figure 4**. The effect of fiber spinning in BCF and the direct drawing in the process with draw ratio of about 4 determines not only a stiffening of the filament but also an increase of max stress (320 MPa) and a relatively high deformation at failure (125%). More peculiar is the orientation in WNW fabric where longitudinal or machine direction and transversal or cross direction determine a different mechanical behavior. Anisotropy of WNW products is very common and usually decreases with the increase of surface density.

This effect is more evident in the creep curve shown in **Figure 5**, where CD sample exhibited not only a higher deformation after 30 mins creep with respect to MD sample (3.1 vs. 2.0%) but also a higher residual after 30 mins recovery (about 0.8 vs. 0.3%).

Correspondingly a higher storage modulus was found for MD sample with respect to CD sample, as shown in **Figure 6**. On the other hand the peak of the polymer glass transition temperature (Tg) remains localized at about 0°C.

The different thermal creep (at 3.5 MPa) of WNW with respect to BCF is reported in **Figure 7**, and it decreases in the order WNW-CD > WNW-MD > BCF. In all cases the deformation starts at about 30°C after the glass transition interval depicted by the loss modulus peak in the interval −15/30°C. As expected, the higher the orientation, the higher the storage modulus, the lower the loss modulus, and consequently the lower the thermal creep.

Figures 8 and **9** show DMTA data of BCF filaments. Storage modulus and thermal creep directly depend on the applied stress.

Moreover, it is evident that static stress of 1 or 7 MPa determines a thermal creep starting from about 30°C, as in the case of WNW with 3.5 MPa (see **Figure 7**). On the other hand, at higher stress of 16 MPa, thermal creep starts at 0°C that correspond to the Tg, measured at the maximum of loss modulus peak.

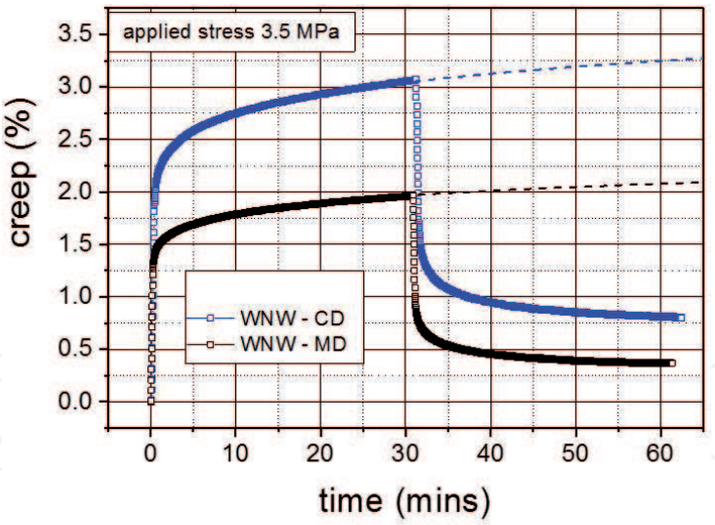

Figure 5.
Comparison of creep curves of WNW fabrics tested in MD and CD directions at 25°C with an applied stress of 3.5 MPa for 30 mins, followed by 30 mins recovery.

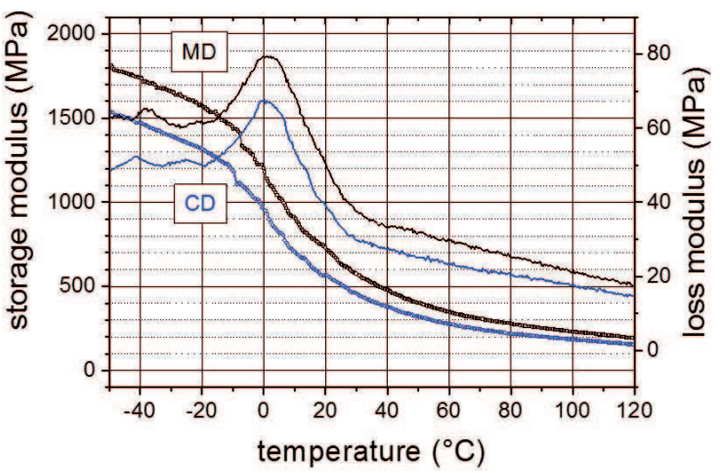

Figure 6.
Dynamic mechanical analysis of WNW fabrics performed at a static stress of 3.5 MPa. Storage modulus (□□□ ○○○) and loss modulus (—— ——) of MD and CD samples are compared.

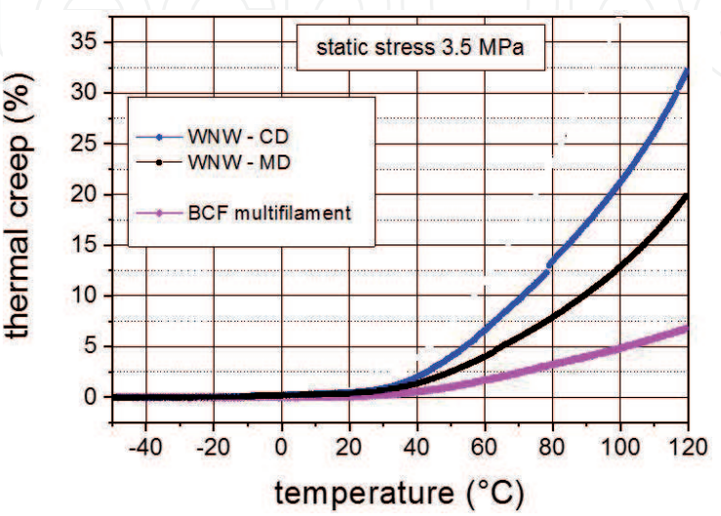

Figure 7.
Thermal creep comparison of WNW fabrics (MD and CD) and BCF filaments as measured by dynamic mechanical analysis with static stress of 3.5 MPa.

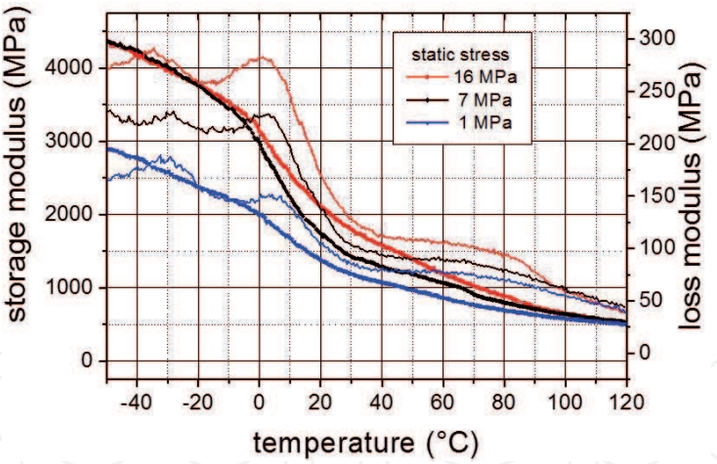

Figure 8.
Dynamic mechanical analysis of BCF filaments performed at different static stresses of 1, 7, and 16 MPa. Storage modulus (▪▪▪◆◆◆▲▲▲) and loss modulus (——).

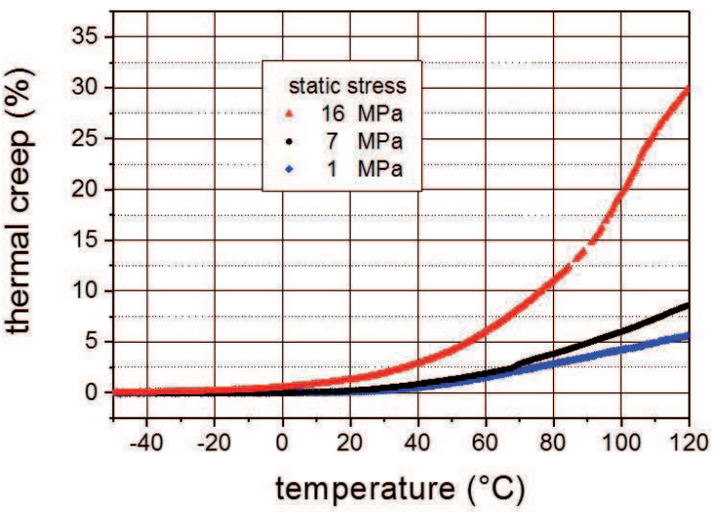

Figure 9.
Comparison of thermal creep measured in dynamic mechanical analysis of BCF filaments performed at different static stresses of 1, 7, and 16 MPa.

Creep curves of BCF filaments at 16 and 78 MPa are compared in **Figure 10**. Experimental data have been interpolated by using a simple exponential model, as previously described [16]. The two parameter K and n formally represent the intensity and the rate of the creep, and they are directly dependent on the applied stress.

Thermal analysis (DSC data) could be useful for a preliminary evaluation of samples. The first heating scan is representative of the products, whereas the cooling step and the second heating scan give information on the polymer. Crystallinity (endothermal peak), the quality of the peak from melting peak and crystallizability of polymer during the cooling step, usually depends on molecular weight. For IM sample melting temperature of 169.2°C and melting enthalpy of 83.2 J/g (crystallinity of 40.2%) were determined. **Tables 2** and **3** show selected data of WNW and BCF samples, respectively. DSC data of various WNW fabrics before and after testing are almost similar.

Thermal analysis of BCF original filaments and after creep or mechanical experiments revealed an interesting result of increased crystallization, in dependence on the well-known phenomenon described as "stress-induced crystallization" [17] or "orientation-induced crystallization" [18] that occurs either in fiber processing or

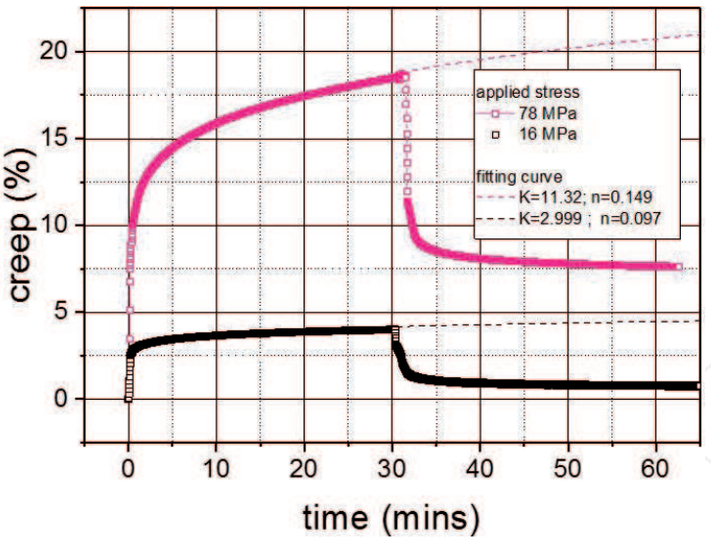

Figure 10.
Comparison of creep curves of BCF filament tested at 25.0°C with different high applied stresses of 11 or 78 MPa for 30 mins, followed by 30 mins of recovery.

WNW	First Scan			Cooling		Second Scan	
	T_{m1} [°C]	ΔH_1 [J/g]	X [%]	T_c [°C]	ΔH_c [J/g]	T_{m2} [°C]	ΔH_2 [J/g]
As received	175.5	84.6	40.5	121.1	95.2	164.2	96.2
MD after creep 3.5 MPa	171.6	84.1	40.2	121.5	96.3	163.4	96.6
CD after creep 3.5 MPa	173.7	84.3	40.3	121.8	95.1	163.6	96.7
MD after failure	170.1	86.2	41.2	121.8	95.7	163.5	95.8
CD after failure	173.1	82.5	39.9	120.1	94.1	165.1	95.2

Crystallinity is calculated according to Eq. (2).

Table 2.
Thermal results of WNW fabrics (melting and crystallization temperature; melting and crystallization enthalpy in the three DSC scans).

BCF	First Scan			Cooling		Second Scan	
	T_{m1} [°C]	ΔH_1 [J/g]	X [%]	T_c [°C]	ΔH_c [J/g]	T_{m2} [°C]	ΔH_2 [J/g]
As received	175.5	74.6	35.7	114.4	90.9	166.6	91.3
After creep 16 MPa	172.9	74.0	35.4	115.1	89.4	165.5	90.7
After creep 78 MPa	172.9	79.4	38.0	115.4	89.5	165.5	91.5
After failure	174.0	108.3	51.8	115.4	89.1	166.0	90.5

Melting and crystallization temperature; melting and crystallization enthalpy in the three DSC scans. Crystallinity is calculated according to Eq. (2).

Table 3.
Thermal results of BCF filaments.

in fiber testing. The residual deformation after creep and recovery was found at 0.7 and 7.5% after loading 16 or 78 MPa, respectively, and correspondently crystallinity of 35 and 38% was measured. It should be noted that crystallinity of BCF filaments increased up to 52% after the failure (strain failure at 125%).

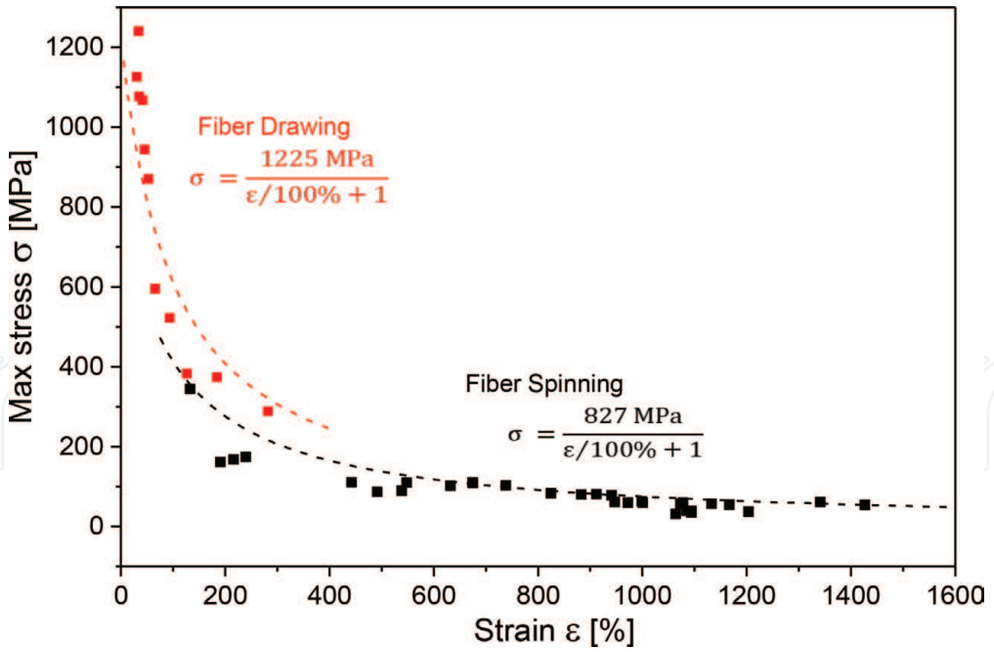

Figure 11.
Comparison of max stress and strain at failure of PP fibers in the two steps of processing, i.e., spinning and drawing. Interpolation curve following the equation proposed in literature [17].

3.2 Case of highly oriented products (fibers)

Single fibers at different levels of drawing were prepared and characterized. **Figure 11** shows the relationship between the max stress and deformation at break that could be interpolated according to the criteria of independence of a total maximum orientation or the network deformation concept [17]. It could be assumed as a direct combination of the orientation obtained in fiber spinning, the extension of the fiber during fiber drawing, and the strain deformation during tensile testing [17]. Experimental results of PP fibers have interpolated separately, distinguishing the spinning step and the drawing step.

The calculated values of 827 and 1225 MPa formally represent the maximum attainable strength in fiber spinning and fiber drawing. It is well evident that 1225 MPa is underestimated, suggesting that various and different phenomena occur during fiber production with different roles and consequences on the ultimate properties.

Moreover, the effect of the filler was also observed and evaluated in drawing, by comparing the modulus and the strength of the fiber as function of draw ratio, as shown in **Figure 12**. The higher the draw ratio, the higher the orientation, and the higher the modulus and the strength, for both PP fiber and composite fibers.

The maximum modulus and strength have been obtained after drawing at draw ratio of DR 15 for both iPP and composite fibers, with values in the range of 8–9 GPa and 900–990 MPa, respectively.

3.3 Texture analysis

Fiber diffraction using transmission images is a powerful technique to analyze polymers especially in fiber or textile form. From a just one diffraction image, it may be possible to get crystal structure information [19, 20], texture [21, 22], and also microstructural features [21]. A strong texture and crystallization may help the crystal structure solution and refinement the same way as the texture is used for crystal structure solutions [22]. The major problem in the quantitative analysis of these transmission images is to account for the texture in a correct way. Simple fiber

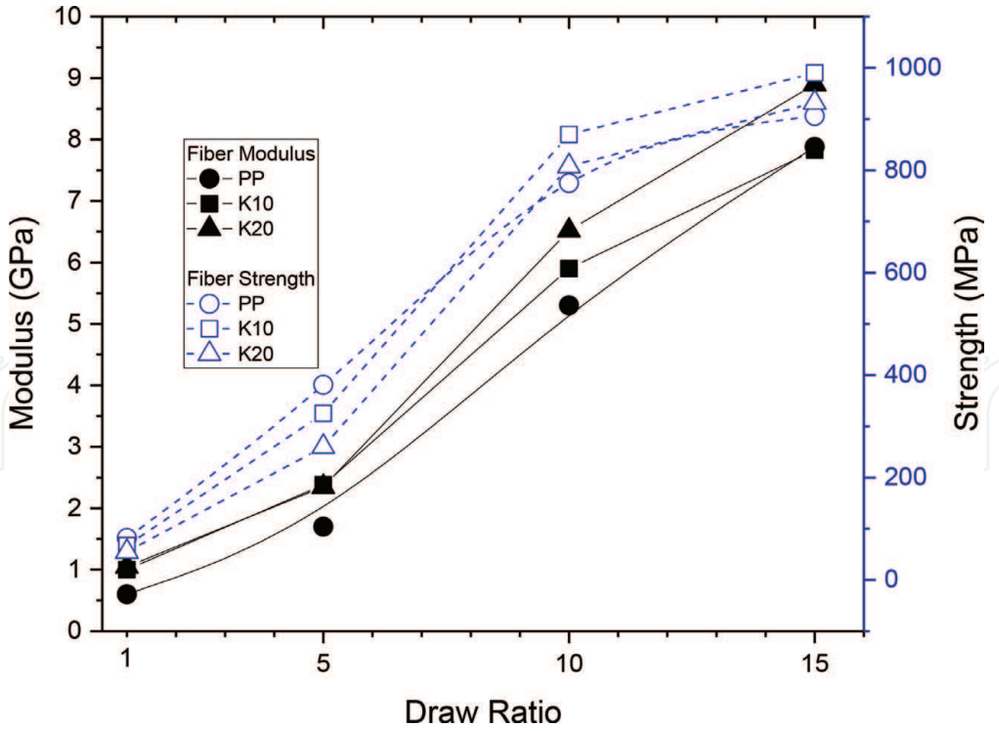

Figure 12.
Modulus and strength of PP fibers and nanocomposites with 10 and 20% of kaolinite as function of draw ratio.

textures can be modeled easily as proven by Ran et al. [23], and in-line analyses can be carried out to monitor the crystallizable behavior of polypropylene fibers. But only one attempt has been made to obtain some rough quantitative information on the texture by Jin et al. [24] for the polypropylene fibers. In this paper we will show a procedure to perform a global diffraction analysis from which we can obtain simultaneously all information from the crystal structure to the orientation distribution function (ODF). The ODF is a function describing the volumetric amount of material with a specific crystallographic orientation in one direction. The procedure is based on the Rietveld texture analysis [25, 26] but using transmission images [20, 21].

To briefly recall the general methodology, the 2D images collected in transmission are transformed in spectra sampling the image in radial slices each one covering a certain diffraction cone angle [27–29]. All the spectra are refined at once in the Rietveld refinement program MAUD [30] using in addition to the crystal structure and size-strain model a texture model to obtain the ODF. In the case of samples in fiber form, the more suitable model is the standard functions [20, 31] as it provides a sufficiently flexible way to represent the ODF with few refined parameters. Instead for smoother texture, like in the case of WNW samples, which we could not model with an ideal standard function, the more flexible spherical harmonic method [25, 31–33] has been used but in the exponential form to ensure a positive function.

Only isotactic polypropylene (iPP) was found in our samples, and for the fiber diffraction images fitting and refinement, we started from the crystal structure determined by Natta et al. [34, 35]. In order to reduce the number of degrees of freedom in our model, we used a bond and angle restraint function for the iPP. This was sufficient to drive our analysis to a unique solution and safely obtain the ODF that was our principal goal.

Figure 13 reports the fitting for the BCF as-span sample. The same analysis procedure was applied also to the strained fibers after creep/recovery at 78 MPa with residual deformation of 7.5% (as shown in **Figure 10**) and after thermal creep in DMTA at 16 MPa with residual deformation of 30% (see **Figure 9**). The experimental diffraction image on the left was transformed by unrolling around the

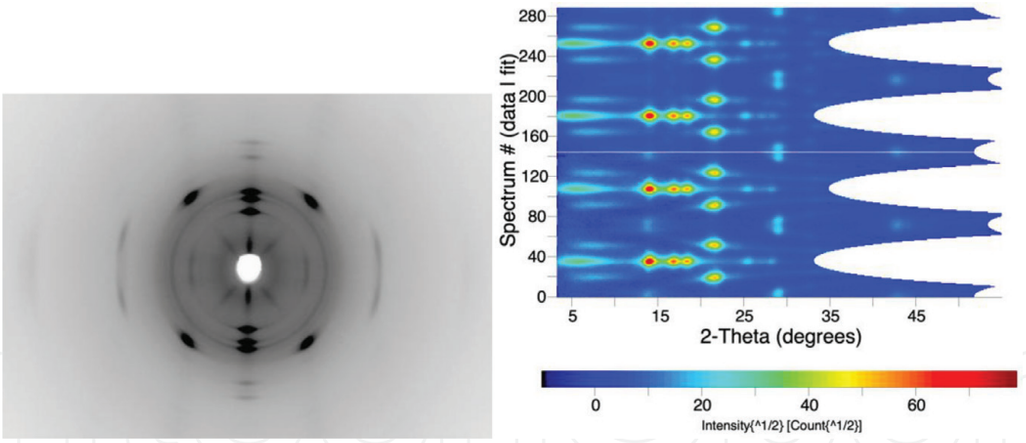

Figure 13.
Original fiber diffraction image for the BCF as-span on the left. Unrolled and fitted data at the end of the analysis on the right. The lower part of the right image (spectrum number from 0 to 143) contains the unrolled experimental data, on the upper part (spectrum number 144 to 287), the calculated patterns. The matching of the two parts indicates a good fitting and correct model.

diffraction center (the white hole) in steps of 2.5° in order to get 144 radial diffraction spectra that were fitted by the program MAUD. **Figure 13**, on the right, shows the result of the fitting. The calculated patterns in the top part well reproduce the unrolled experimental spectra in the bottom. The longer spots at low angles, and visible in the image on the right as radial short strings, are due to the diffraction of the bremsstrahlung that was also included in the pattern modeling. In the unrolled map on the right, the presence of sharper spots vertically means sharper texture. Instead, sharper spots horizontally correspond to a better crystallization of the fibers/compound.

In **Figure 14** we have recalculated some of the pole figures from the ODFs obtained for the three BCF samples. Pole figures, being 2D, are somehow more convenient to visualize the texture characteristics. All three different fibers show the same kind of texture: the fiber axis is parallel to the normal to the pole figures, and a perfect fiber symmetry was found for the (100) axis. For the texture analysis, we were obliged to use the monoclinic c-setting for the iPP instead of the more common b-setting. The usual (001) fiber axis becomes the (100) in our case, because of the different cell conventions used. The texture sharpness does not change significantly between the as-span and strained fibers at room temperature, but there is a strong increase in fiber alignment after thermal creep. In fact the fiber spread obtained from the fitting was 15 ± 1° for the as-span and 17 ± 1° for the room temperature creep but becomes 9 ± 1° for the fibers after creep in DMTA up to 120°C (see **Figure 9**). Also the mean crystallite sizes, as measured from the analysis, increase from 14 to 19 nm with the thermal creep, but it is not affected by the creep at room temperature. These findings are in agreement with the residual deformation of BCF filament, i.e., 30% after thermal creep (**Figure 9**) and 7.5% after creep/recovery (**Figure 10**).

For the WNM samples, for which we show only one experimental diffraction image and its fitting in **Figure 15**, the results of the texture analysis for the three samples, as received and after creep in MD and CD directions, are shown in **Figure 16**. The texture is weaker than in the previous BCF case and it is not a fiber one. The machine and cross directions show a slightly different fiber alignment that gives result to a different texture when subjected to creep in their respective direction. The texture sharpness increases a bit and more for the machine direction, as it was showing a more favorable alignment of the fibers from the beginning.

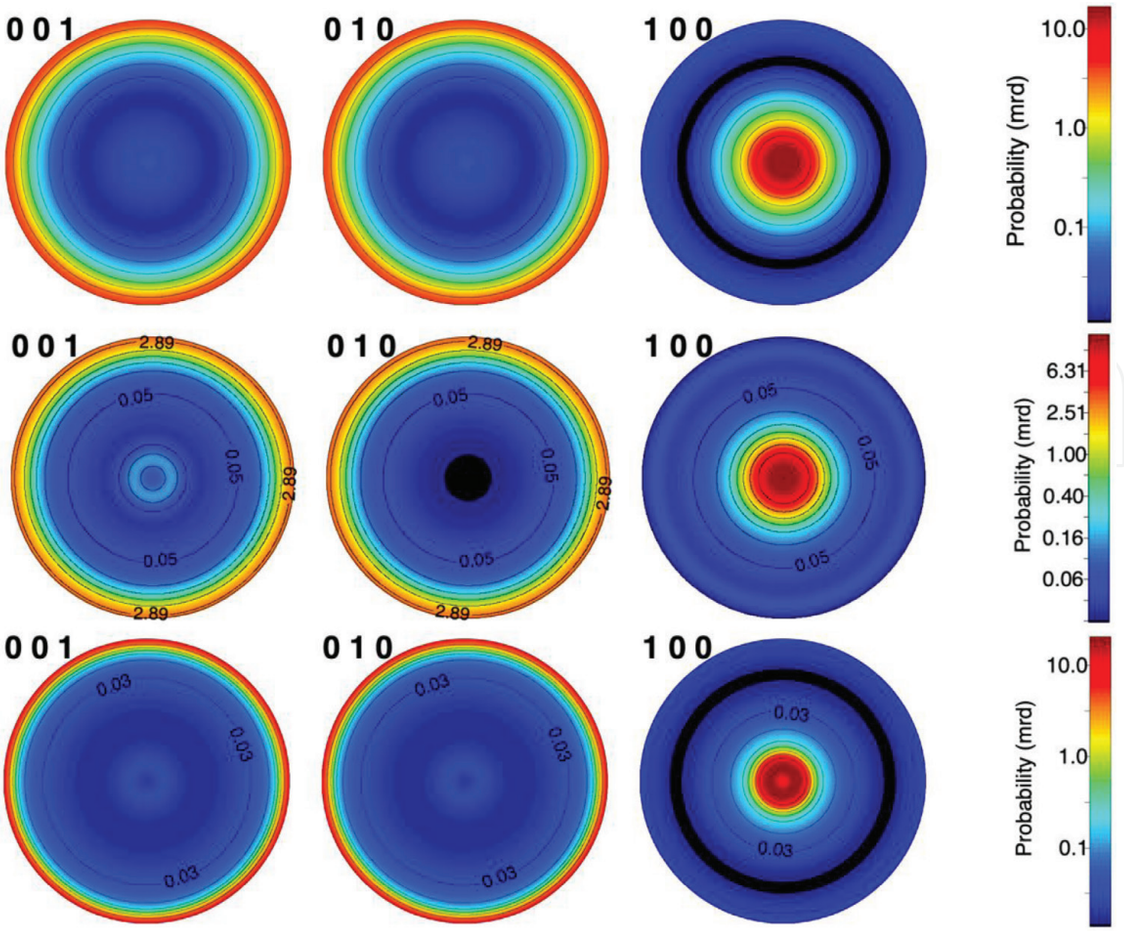

Figure 14.
Recalculated pole figures for BCF fibers (from top): as-span, after creep at 78 MPa (room temperature) and after thermal creep at 16 MPa. Only after creep at high temperature we notice an increase in the crystallographic alignment of the fibers. The fiber sample direction corresponds to the normal to the pole figures.

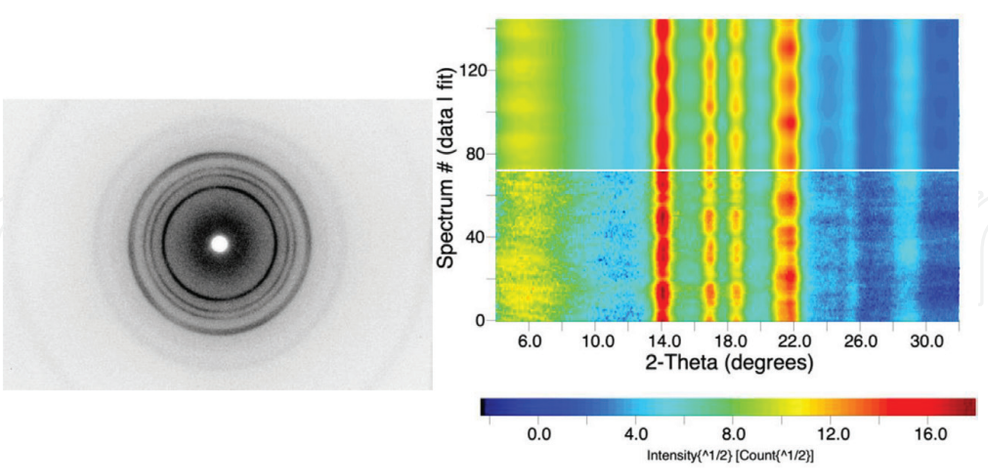

Figure 15.
Original fiber diffraction image (left) and unrolled and fitted patterns (right) for the WNW sample. The texture is much smoother with respect to the drawn fiber samples. With respect to **Figure 13**, *the uncomplete 2Θ range has been cut to enhance low-angle features.*

Finally, we analyzed in fiber diffraction also one sample containing kaolinite. The analysis was more difficult in this case as two textured phases are present. Again, kaolinite shows a high density of modulated planar defects and strong compression in the plane normal to the fibers axis.

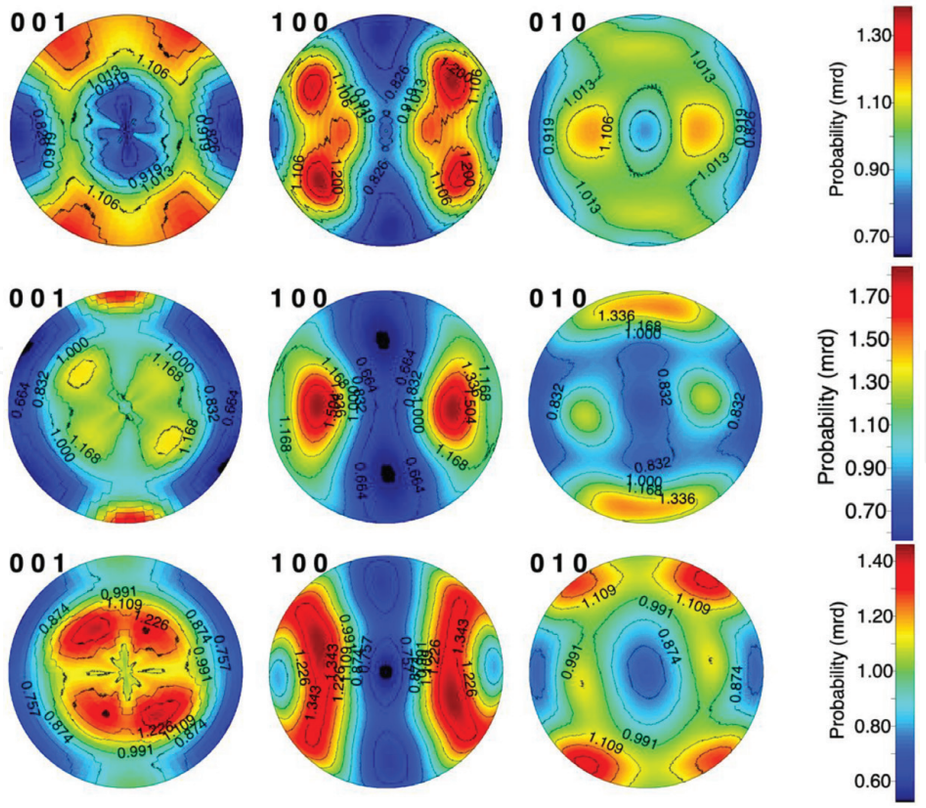

Figure 16.
Recalculated pole figures for WNW samples (from top): as prepared, after creep in machine direction, and after creep in cross direction. The pole figures' horizontal direction corresponds to the normal to the WNW in-plane tissue. The creep direction is normal to the pole figures for MD and vertical for CD.

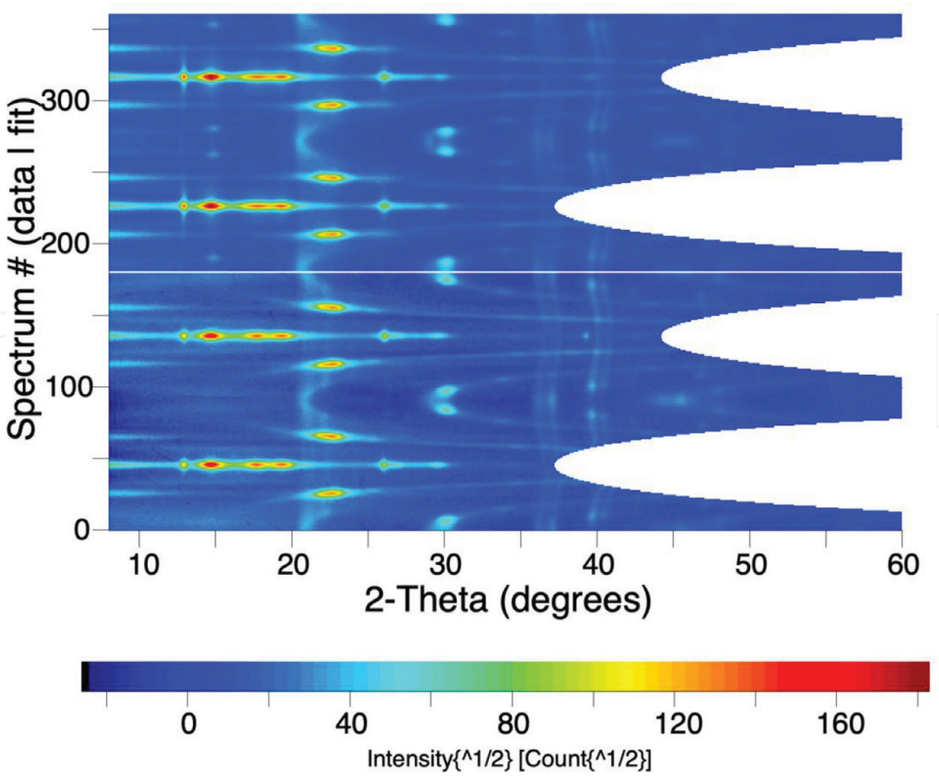

Figure 17.
Rietveld fitting of the unrolled diffraction image for the sample K10. The spectrum number corresponds to a pattern integrated radially every 2° in the circumferential direction starting from the horizontal plane. There are 180 experimental integrated patterns in the lower part and 180 recalculated patterns in the upper part. The waving vertical lines correspond to the kaolinite diffraction interplanar spacings in compression in the plane perpendicular to the fibers.

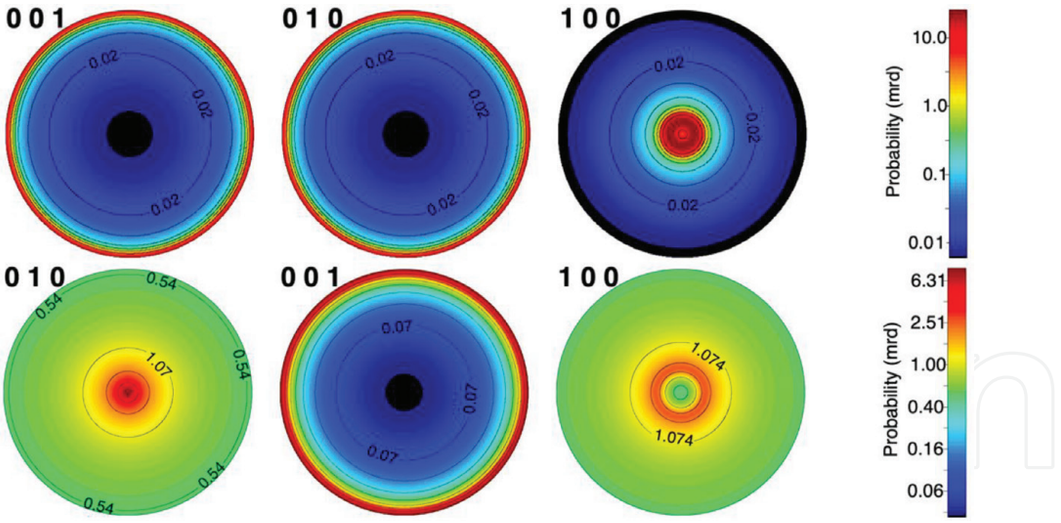

Figure 18.
Recalculated pole figures of iPP (top) and kaolinite (bottom) resulting from the Rietveld texture fitting. The fiber direction is normal to the pole figures.

To correctly model the unrolled diffraction patterns, as reported in **Figure 17**, we had to derive a modulated planar defect model for kaolinite starting from a previous turbostratic model [36]. This modulated defect structure has been tested by analyzing the powder diffraction pattern of the same kaolinite used as filler in the fibers.

The fitting of the fiber diffraction, for the iPP with 10 wt% kaolinite at DR = 10, is reported in **Figure 17**. The iPP texture and microstructure characteristics are similar to the BCF, especially the one after thermal creep, and by difference with **Figure 13**, the reader may recognize which ones are the diffraction spots and lines of kaolinite. Kaolinite shows a high compression state perpendicular to the fiber axis corresponding to about 0.8% equivalent elastic strain. This extremely high deformation is probably induced by the fiber drawing and the intercalation with kaolinite. By the strong texture, the deformation mainly belongs to the (001) kaolinite basal plane (perpendicular to the plane) that is also the intercalation and faulted plane.

From the crystallization point of view, the iPP is similar to the BCF after thermal creep (17 nm for the mean crystallite sizes), and kaolinite is arranged in packets of about 50 nm perpendicular to the basal plane.

Figure 18 is showing the recalculated pole figures for the iPP and kaolinite. The fiber spread of the iPP corresponds to 7.3 ± 0.5°, and so kaolinite contributes to the alignment of the fibers reaching a texture even sharper than the BCF after thermal creep. From the kaolinite pole figures, we can deduce that the (001) basal plane is distributed normal to the fiber axis but in a perfect fiber texture.

Finally, from the analysis of the fiber diffraction image, we can measure also the amount of kaolinite, and thanks to the proper modeling, including texture and strain effects, the refined amount was 10.7 wt% that is very close to the amount inserted (10 wt%).

4. Conclusions

It can be concluded that polymer processing directly affects mechanical properties of iPP fiber-like products, as observed in the case of WNW fabrics and fibers, both BCF and monofilaments. The higher the orientation, the higher the modulus and the strength, the lower the deformation at break, and the higher the creep resistance. No particular variation of crystallinity of specimen before and after creep and fracture test was detected by DSC analysis, except for BCF after failure.

In the case of composite fibers, the improvement in mechanical properties of monofilament is mainly dependent on the fiber drawing, whereas only a marginal contribute of kaolinite content has been observed. For instance, the processing-drawing with draw ratio of 10 produced monofilaments of iPP and kaolinite composite with modulus and strength in the range of 5.5–6.5 GPa and of 770–870 MPa, respectively.

From the texture analyzed by X-ray, we can notice that the fiber alignment is only affected by the creep at high temperature. Stretching the fibers at room texture has a negligible effect on the texture. The situation may be different for the WNW, where the fibers have a higher mobility and the stress can change their orientation, also at lower temperatures.

In addition, from this work we can conclude that the mechanical properties are highly correlated to the texture and reverse. The fibers after thermal creep, which are showing the higher residual deformation, show also a higher increase in the texture.

Acknowledgements

Authors wish to thank Aquafil SpA (Arco, TN, Italy) and Texbond Spa (Rovereto, TN, Italy) for providing BCF filaments and woven non-woven fabrics, respectively. Moreover, the authors acknowledge N. Soave for injection molding and I. Dabrowska, D. Lorenzi, and K.T. Chaka for fiber spinning.

This research received no external funding.

Conflict of interest

The authors declare no conflict of interest.

Dedication/other declarations

This work is dedicated to the memory of Prof. József Karger-Kocsis (†December 13, 2018).

Appendices and nomenclature

BCF	bulk continuous filament
CD	cross direction
DM(T)A	dynamic mechanical (thermal) analysis
DR	draw ratio
DSC	differential scanning calorimetry
FS	fiber spinning
IM	injection molding
MAUD	material analysis using diffraction, software for X-ray analysis
MD	machine direction
TEM	transmission electron microscopy
Tg	glass transition temperature
XRD	X-ray diffraction
WNW	woven non-woven fabric
ODF	orientation distribution function

DOI: http://dx.doi.org/10.5772/intechopen.85554

IntechOpen

Author details

Luca Fambri* and Luca Lutterotti
Department of Industrial Engineering, University of Trento, Italy

*Address all correspondence to: luca.fambri@unitn.it

References

[1] Kutsch O. Market Study: Polypropylene. 4th Ed. Available from: http://www.ceresana.com/en/marketstudies/plastics/polypropylene/ [Accessed: 18 October 2018]

[2] Plastics Europe. Plastics-The Facts 2018. An Analysis of European Plastics Production, Demand and Waste Data. 2018. 25 p. Available from: http://www.plasticseurope.org/download_file/force/2367/181 [Accessed: 13 December 2018]

[3] Moore EP. Polypropylene Handbook: Polymerization, Characterization, Properties, Processing, Applications. Munich: Hanser Publishers; 1996. pp. 303-348. ISBN: 3446181768

[4] Karian HG. Handbook of Polypropylene and Polypropylene Composites. New York: Marcel Dekker; 1999. pp. 15-37. ISBN: 0824719492

[5] Fambri L, Lorenzi D, Masarati E, Costantini E. Chapter 12: High load polypropylene composites. In: Silva LP, Barbosa EF, editors. Polypropylene: Synthesis, Applications and Environmental Concerns. Happauge New York: Novascience Publishers; 2013. pp. 261-284. ISBN: 978-1-62417-152-9. Available from: https://www.novapublishers.com/catalog/product_info.php?products_id=42212

[6] American Standard Testing Materials ASTM D1238-10: Standard Test Method for Melt Flow Rates of Thermoplastics by Extrusion Plastometer

[7] Tripathi D. Practical Guide to Polypropylene. Shawbury, UK: Rapra Technology Ltd; 2002. pp. 75-84. ISBN-10: 1859572820

[8] Wishman M, Hagler GE. Polypropylene fibers. In: Lewin P, Pearce EM, editors. Handbook of Fiber Science and Technology Fiber Chemistry. Vol. 4. New York: Marcel Dekker; 1985. pp. 371-497. ISBN: 0-8247-7335-7

[9] Mather RR. The structure of polyolefin fibres. In: Eichhorn SJ, Hearle JWS, Jaffe M, Kikutani T, editors. Handbook of Textile Fiber Structure. Vol. 1. Cambridge, UK: Woodhead Publishing; 2009. pp. 276-304. ISBN: 9781845693800

[10] Kunugi T. High-modulus and high-strength polypropylene fibers and films. In: Karger-Kocsis J, editor. Polypropylene an A-Z Reference. Dordrecht The Netherlands: Kluwer Academic Publishers; 1999. pp. 295-300. ISBN: 0412802007

[11] Fujiyama M. Higher order structure of injection-molded polypropylene. In: Karger-Kocsis J, editor. Polypropylene Structure, Blends and Composites. Vol. 1. London: Chapman & Hall; 1995. pp. 167-204. ISBN 0412802007

[12] Feng B, Fuming L, Calhoun BH, Quirk RP, Cheng SZD. Physical constants of poly(propylene). In: Brandrup J, Immergut EH, Grulke EA, editors. Polymer Handbook. 4th ed. New York: Wiley; 1999. p. V-21. ISBN 0-471-16628-6

[13] European Disposables and Nonwovens Association (EDANA) [Internet]. 1999. Available from: http:///www.edana.org/discover-nonwovens/how-they're-made/formation [Accessed: 30 November 2018]

[14] Bertamini L, Caldara M, Giacomelli G, Pontarin LM, Fambri L, Casagranda A. New fibres for floor-covering and textile applications. Chemical Fibers International. 2006;**1**:28-35

[15] Fambri L, Dabrowska I, Ceccato R, Pegoretti A. Effects of fumed silica

and draw ratio on nanocomposite polypropylene fibers. Polymers. 2017;**9**:41. DOI: 10.3390/polym9020041

[16] Dabrowska I, Fambri L, Batistella M, Lopez-Cuesta JM. Compounding and spinning of polypropylene nanocomposites with kaolinite. In: Proceedings of 16th Eur. Conf. On Comp. Materials (ECCM16); 22-26 June 2014; Seville, Spain; ID 725. 2014. pp. 1-8

[17] Beyreuther R, Brunig H, editors. Dynamics of Fibre Formation and Processing. Heidelberg: Springer; 2007. pp. 65-81. DOI: 10.1007/978-3-540-46223-1

[18] Jinan C, Kikutani T, Takaku A, Shimizu J. Nonisothermal orientation-induced crystallization in melt spinning of polypropylene. Journal of Applied Polymer Science. 1989;**37**(9):2683-2697. DOI: 10.1002/app.1989.070370919

[19] Chatani Y, Maruyama H, Noguchi K, Asanuma T, Shiomura T. Crystal structure of the planar zigzag form of syndiotactic polypropylene. Journal of Polymer Science Part C: Polymer Letters. 1990;**38**:393-398

[20] Lutterotti L, Bortolotti M, Fambri L. Crystal structure and texture refinement of polymers from diffraction images. Acta Crystallographica. 2005;**A61**:C391-C392

[21] Lutterotti L, Bortolotti M, Ischia G, Lonardelli I, Wenk HR. Rietveld texture analysis from diffraction images. Zeitschrift für Kristallographie Supplements. 2007;**26**:125-130

[22] Wessel T, Baerlocher C, McCusker LB. Single-crystal-like diffraction data from polycrystalline materials. Science. 1999;**284**:477-479

[23] Ran S, Zong X, Fang D, Hsiao BS, Chu B, Ross RJ. Novel image analysis of two-dimensional X-ray fiber diffraction patterns: Example of a polypropylene fiber drawing study. Journal of Applied Crystallography. 2000;**33**:1031-1036

[24] Jin Y, Rogunova M, Hiltner A, Baer E, Nowacki R, Galeski A, et al. Structure of polypropylene crystallized in confined nanolayers. Journal of Polymer Science Part B: Polymer Physics. 2004;**42**:3380-3396

[25] Ferrari M, Lutterotti L. Method of simultaneous determination of anisotropic residual stresses and texture by X-ray diffraction. Journal of Applied Physics. 1994;**76**(11):7246-7255

[26] Matthies S, Lutterotti L, Wenk HR. Advances in texture analysis from diffraction spectra. Journal of Applied Crystallography. 1997;**30**:31-42

[27] Lutterotti L, Matthies S, Wenk HR, Schultz AS, Richardson JW Jr. Combined texture and structure analysis of deformed limestone from neutron diffraction spectra. Journal of Applied Physics. 1997;**81**:594-600

[28] Lutterotti L, Vasin R, Wenk HR. Rietveld texture analysis from synchrotron diffraction images: I. Calibration and basic analysis. Powder Diffraction. 2014;**29**(1):76-84

[29] Wenk HR, Lutterotti L, Kaercher P, Kanitpanyacharoen W, Miyagi L, Vasin R. Rietveld texture analysis from synchrotron diffraction images: II. Complex multiphase materials and diamond anvil cell experiments. Powder Diffraction. 2014;**29**(3):220-232

[30] Lutterotti L. Total pattern fitting for the combined size-strain-stress-texture determination in thin film diffraction. Nuclear Instruments and Methods in Physics Research B. 2010;**268**:334-340

[31] Matthies S, Vinel GW, Helming K. Standard Distribution in Texture Analysis. Berlin: Akademie-Verlag; 1987

[32] Bunge HJ. Texture Analysis in Materials Science, Mathematical Methods. Berlin: Akademie-Verlag; 1969. ISBN: 0-408-10642-5

[33] Popa NC. Texture in Rietveld refinement. Journal of Applied Crystallography. 1992;**25**:611-616

[34] Natta G, Corradini P. Structure and properties of isotactic polypropylene. Nuovo Cimento, Supplemento. 1960;**15**:40-51

[35] Brückner S, Meille SV, Petraccone V, Pirozzi B. Polymorphism in isotactic polypropylene. Progress in Polymer Science. 1991;**16**:361-404

[36] Lutterotti L, Voltolini M, Wenk HR, Bandyopadhyay K, Vanorio T. Texture analysis of a turbostratically disordered Ca-montmorillonite. American Mineralogist. 2010;**95**(1):98-103